

Fig. 1: Compressive CSI estimation based on the linear P2D estimator. First, downlink pilots are used to estimate a sparse, downsampled frequency domain CSI estimate of size $M_f \ll N_f$. Then, the P2D estimator, $\mathbf{Q}_{N_t}^\dagger$ of (2), is applied to establish an accurate truncated delay domain CSI estimate. After P2D estimation, a learnable UE (BS) transform $f(x)$ ($g(x)$) is used to compress and decode the feedback, respectively. Finally, the delay domain estimate can be transformed into the frequency domain for precoding.

$\tilde{\mathbf{h}}_a \in \mathbb{C}^{N_f}$, which is obtained using a pilot frequency selection matrix, $\mathbf{P} \in [0, 1]^{M_f \times N_f}$ where each row is a one-hot vector. Thus, the matrix-vector product $\tilde{\mathbf{h}}_j = \mathbf{P}\tilde{\mathbf{h}}_j \in \mathbb{C}^{M_f}$ represents a downsampled version of the antenna vector $\tilde{\mathbf{h}}_a$.

While the discussion so far has focused on spatial-frequency CSI, most works in compressive CSI estimation opt to use the angular-delay domain CSI, $\tilde{\mathbf{H}}$, which exhibits greater sparsity and is more amenable to compression than the spatial-frequency domain [5]. Such works presume that the angular-delay domain data are readily available at the UE, but in reality, the UE only has access to the CSI estimated via pilots (i.e., the downsampled frequency-spatial CSI matrix $\tilde{\mathbf{H}}$).

III. LINEAR PREDICTION OF DELAY-DOMAIN CSI VIA FREQUENCY-DOMAIN PILOTS

Using the limited number of frequency domain pilots available at the UE, we can estimate the truncated delay domain data. This delay domain estimate is directly compatible with the commonly used CSI basis in prior deep learning based CSI compression works [5], [11], which have demonstrated high estimation accuracy under substantial compression.

A. Frequency Domain Downsampling

Consider the case where downsampling is performed along the frequency axis such that M_f subcarriers of the original N_f subcarriers remain. Downsampling is done by applying the pilot matrix $\mathbf{P} \in \mathbb{C}^{M_f \times N_f}$ to the frequency domain vector \mathbf{h}_f , resulting in the pilot vector $\tilde{\mathbf{h}}_f \in \mathbb{C}^{M_f}$. Note that \mathbf{h}_f is one of the rows of the spatial-frequency matrix \mathbf{H} .

To relate the frequency and delay domain, denote the Fast Fourier Transform (FFT) dual,

$$\mathbf{F}_{N_f} \mathbf{h}_d = \mathbf{h}_f.$$

Applying the pilot matrix to both sides, we have

$$\begin{aligned} \mathbf{P}\mathbf{F}_{N_f} \mathbf{h}_d &= \mathbf{P}\mathbf{h}_f \\ \mathbf{Q}\mathbf{h}_d &= \tilde{\mathbf{h}}_f, \end{aligned}$$

where $\mathbf{Q} = \mathbf{P}\mathbf{F}_{N_f}$. Given the sparsity of CSI in the delay domain, we may truncate \mathbf{Q} to the first N_t columns and restrict our attention to the truncated delay domain vector, $\tilde{\mathbf{h}}_d \in \mathbb{C}^{N_t}$,

$$\mathbf{Q}_{N_t} \tilde{\mathbf{h}}_d = \tilde{\mathbf{h}}_f.$$

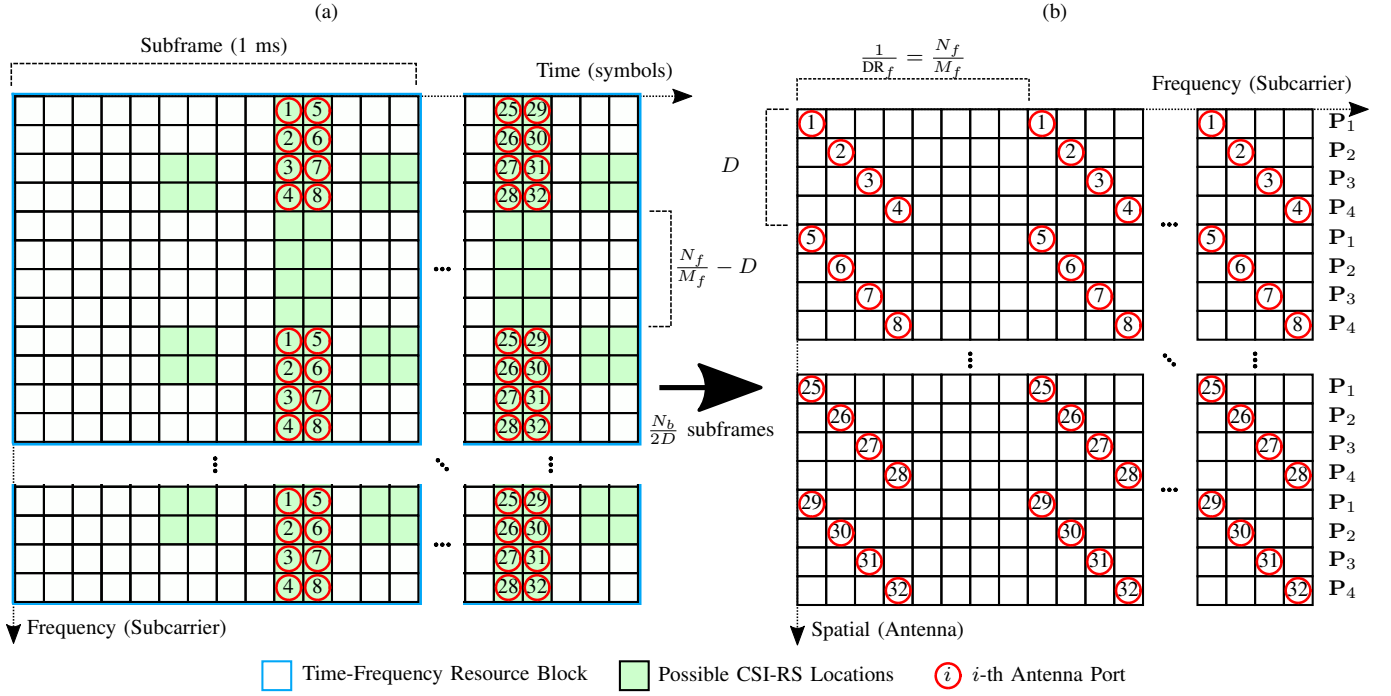


Fig. 2: (a) LTE Resource Blocks and CSI-RS locations where antenna port pilots are allocated. (b) Schematic for diagonal pilots with relevant parameters, size of diagonal D and frequency downsampling ratio DR_f . In this diagram, $N_b = 32$, $D = 4$, $DR_f = \frac{1}{8}$. The pilot matrix P_j indicates the downsampling pattern for the j -th element of the diagonal pattern. The number of subframes necessary to populate (b) is inversely proportional to D .

To solve for $\bar{\mathbf{h}}_d$, we perform the pseudoinverse $\mathbf{Q}_{N_t}^\dagger$,

$$\bar{\mathbf{h}}_d = \mathbf{Q}_{N_t}^\dagger \bar{\mathbf{h}}_f \quad (2)$$

$$= (\mathbf{Q}_{N_t}^H \mathbf{Q}_{N_t})^{-1} \mathbf{Q}_{N_t}^H \bar{\mathbf{h}}_f \quad (3)$$

This solution relies solely on the downsampling matrix, \mathbf{P} , and the FFT matrix, \mathbf{F}_{N_f} . We call this solution the pilots-to-delay (P2D) estimator since it allows us to estimate the truncated delay domain CSI ($\bar{\mathbf{H}}$) based on sparse frequency domain pilots. Figure 1 shows where the P2D estimator fits into the overall CSI feedback and estimation process.

In contrast with a ‘‘Compression Ratio (CR)’’ that is typically reported in the feedback stage, the P2D estimator is associated with a ‘‘Frequency Downsampling Ratio (DR_f),’’ which is given as

$$\text{Frequency Downsampling Ratio (DR}_f) = \frac{M_f}{N_f}. \quad (4)$$

B. Diagonal Pilot Patterns for LTE Compatibility

In the LTE specification, downlink pilots for antenna ports are allocated to specific resource elements (CSI-RS) in the time-frequency resource grid [12]. For a MIMO array, the different antenna ports are allocated to CSI-RS locations in the resource grid, and multiple subframes might be necessary to acquire the entire downsampled CSI matrix. The number of subframes necessary depends on two design parameters: 1) the size of the diagonal pattern, D , and 2) the frequency downsampling ratio, DR_f .

Algorithm 1 Pilots to Delay (P2D) Estimator for Diagonal Pilot Pattern

- 1: **Input:** Pilot spatial-frequency CSI, $\bar{\mathbf{H}} \in \mathbb{C}^{N_b \times M_f}$
- 2: **Input:** Diagonal parameter, D
- 3: **Initialize:** Spatial-delay CSI, $\bar{\mathbf{H}} \in \mathbb{C}^{N_b \times N_t}$
- 4: **Initialize:** Angular-delay CSI, $\bar{\mathbf{H}} \in \mathbb{C}^{N_b \times N_t}$
- 5: **for** $i = 1, 2, \dots, N_b$ **do**
- 6: # **Index for j -th pilot matrix**
- 7: $j = ((i - 1) \bmod D) + 1$
- 8: # **Apply P2D to i -th pilot subcarrier**
- 9: $\bar{\mathbf{h}}_f(i) = \bar{\mathbf{H}}(i, :)$
- 10: $\bar{\mathbf{H}}(i, :) = \mathbf{Q}_{j, N_t}^\dagger \bar{\mathbf{h}}_f(i)$
- 11: **end for**
- 12: # **Convert spatial domain to angular**
- 13: $\bar{\bar{\mathbf{H}}} = \text{FFT}(\bar{\mathbf{H}})$
- 14: **Return** $\bar{\bar{\mathbf{H}}}$

Figure 2a illustrates our proposed pilot allocation for an LTE time-frequency resource grid, and Figure 2b shows the resulting downsampling pattern in the spatial-frequency domain. Based on Figure 2, the benefit of diagonal pilot patterns becomes apparent, as the number of subframes needed to acquire the downsampled CSI matrix, $\bar{\mathbf{H}}$ at the UE decreases with increasing D . For example, the given diagonal size $D = 4$ requires 4 subframes (ms) to acquire $\bar{\mathbf{H}}$, while $D = 1$ (i.e., no

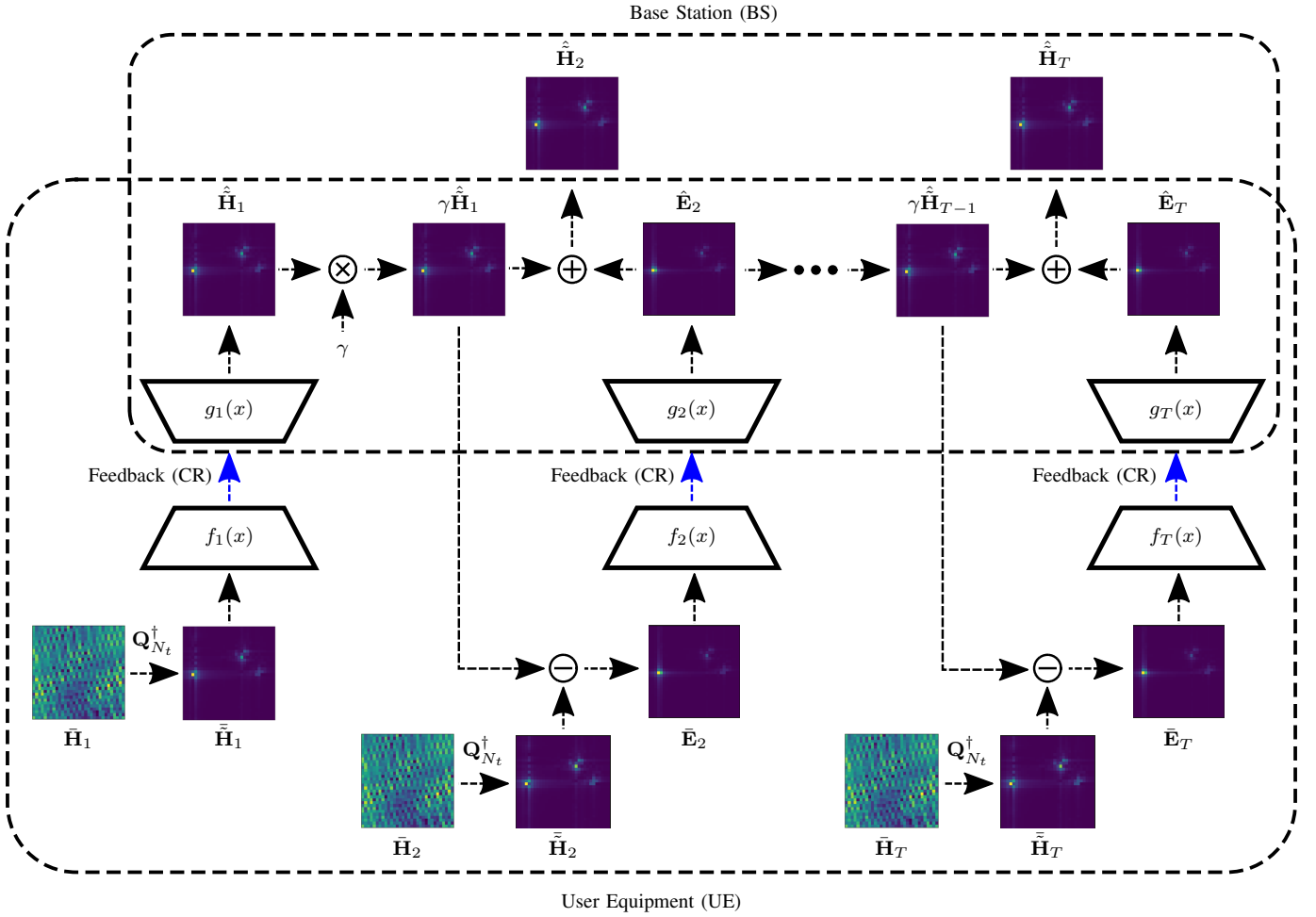


Fig. 3: Diagram of a CSI estimation network using compressed differential feedback based on the linear P2D estimator. First, downlink pilots are used to estimate a downsampled frequency domain CSI estimate, $\tilde{\mathbf{H}}_t \in \mathbb{C}^{N_b \times M_f}$ where $M_f \ll N_f$ at the t -th timeslot. Then, the P2D estimator, $\mathbf{Q}_{N_t}^\dagger$ of (2), is applied to estimate $\tilde{\mathbf{H}}_t$. After P2D estimation, the learnable transforms $f_t(x)$ and $g_t(x)$ are used to compress and decode the feedback, respectively. For $t = 1$, the encoder/decoder are applied directly to $\tilde{\mathbf{H}}_1$. In all subsequent timeslots ($t > 1$), the differential term \mathbf{E}_t is compressed and fed back.

diagonal pattern or vertical columns of pilots) would require 16 subframes (ms) to acquire $\tilde{\mathbf{H}}$.

To utilize the P2D estimator while using diagonal pilot patterns, it is necessary to account for different pilot matrices, \mathbf{P}_j for $j \in [1, \dots, D]$, used with different antennas. These different pilot matrices result in D different P2D estimators, $\mathbf{Q}_{j, N_t}^\dagger$. Algorithm 1 outlines the process for acquiring $\tilde{\mathbf{H}}$ by applying the P2D estimators to $\tilde{\mathbf{H}}$.

C. Regularization of P2D Estimator

The pseudoinverse matrices $\mathbf{Q}_{N_t}^\dagger$ are typically ill-conditioned given the sparsity of the pilot selection matrices \mathbf{P} . Consequently, the P2D estimator benefits from regularization of the matrix $\mathbf{Q}_{N_t}^H \mathbf{Q}_{N_t}$. This can be done via off-diagonal regularization (ODIR), where all off-diagonal elements are scaled down by a fixed constant. Denote \mathbf{A} as a matrix to

be regularized where $A(i, j)$ is the element in the i -th row and j -th column. The ODIR version of this matrix is

$$A(i, j) = \begin{cases} A(i, j) & i = j \\ \frac{A(i, j)}{1+\delta} & i \neq j \end{cases} \quad (5)$$

IV. DIFFERENTIAL ENCODING VIA LEARNED COMPRESSED SENSING

To further improve the accuracy of CSI estimation under the P2D estimator, we can exploit the temporal coherence of the channel. Under typical circumstances, the channel does not change substantially for a given window of time, i.e. the coherence interval. Exploiting this coherence is beneficial from an information theoretic point of view [11]. Denote two subsequent timeslots within a coherence interval as t_1 and t_2 , the entropy of the CSI at t_1 as $H(\tilde{\mathbf{H}}_1)$, and the conditional entropy of the CSI at t_2 given t_1 as $H(\tilde{\mathbf{H}}_2 | \tilde{\mathbf{H}}_1)$.

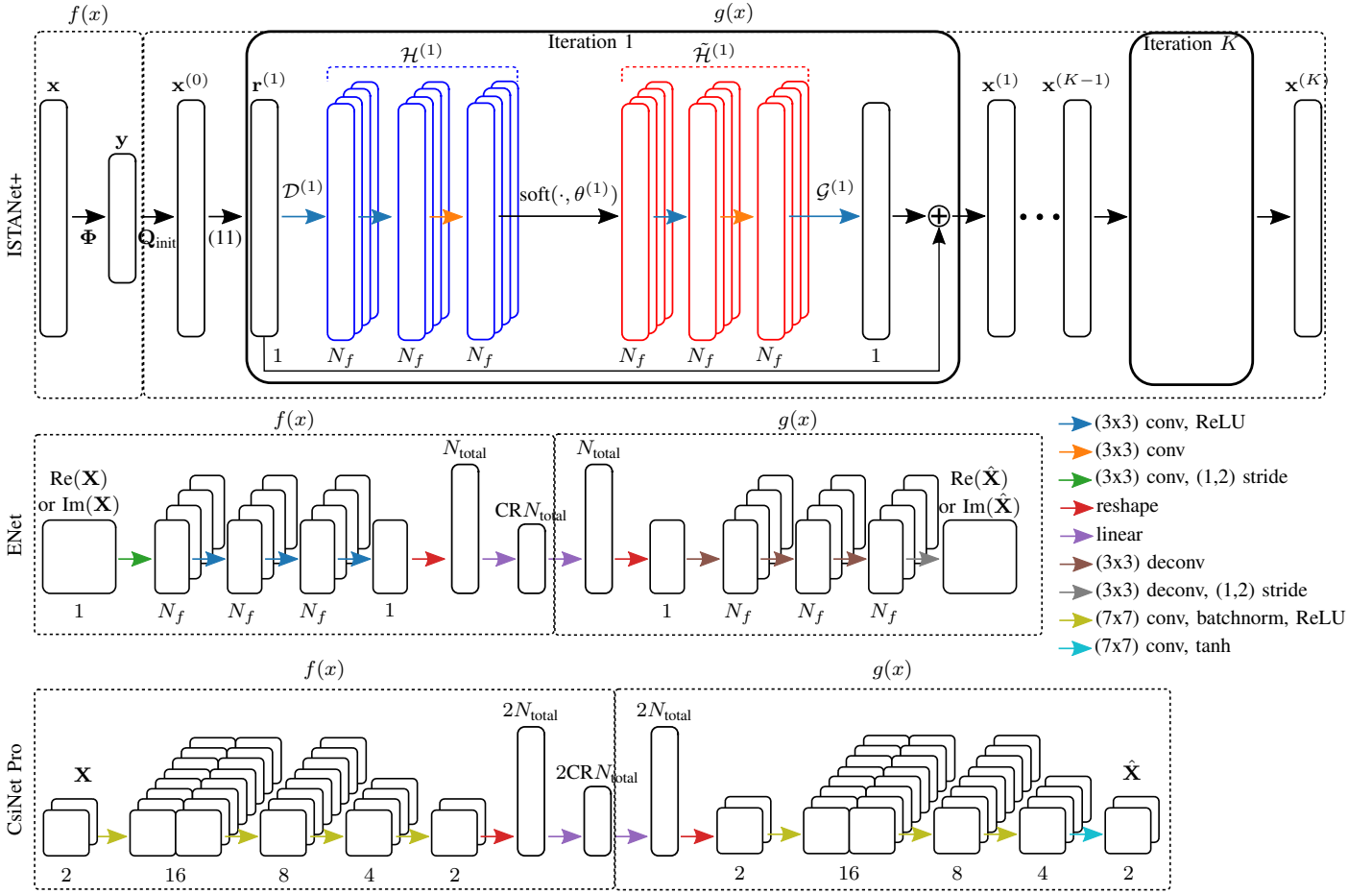


Fig. 4: Compressive CSI estimation architectures used in this work. $f(x)$ denotes the encoder, and $g(x)$ denotes the decoder. $N_{\text{total}} = N_b N_t$ is the size of the real or imaginary channel.

Prior work in time-varying CSI estimation has demonstrated that the conditional entropy is always lower than the entropy [11], i.e.,

$$H(\tilde{\mathbf{H}}_2 | \tilde{\mathbf{H}}_1) \leq H(\tilde{\mathbf{H}}_1). \quad (6)$$

A reduction in entropy means a reduction in the rate of the compressed feedback, highlighting the utility of differential feedback. Instead of directly encoding/decoding the CSI (e.g., $\hat{\mathbf{H}}_t = g(f(\tilde{\mathbf{H}}_t))$), we propose to encode/decode the difference,

$$\begin{aligned} \bar{\mathbf{E}}_t &= \tilde{\mathbf{H}}_t - \check{\mathbf{H}}_t \\ &= \tilde{\mathbf{H}}_t - \gamma \hat{\mathbf{H}}_{t-1}, \end{aligned} \quad (7)$$

where $\check{\mathbf{H}}_t = \gamma \hat{\mathbf{H}}_{t-1}$ is the least-squares estimate for $\tilde{\mathbf{H}}_t$ based on the estimate in the previous timeslot, $\hat{\mathbf{H}}_{t-1}$. We apply the encoding/decoding process to the error term, $\hat{\mathbf{E}}_t = g_t(f_t(\bar{\mathbf{E}}_t))$, and the resulting CSI estimate can be written as

$$\hat{\mathbf{H}}_t = \hat{\mathbf{E}}_t + \gamma \hat{\mathbf{H}}_{t-1}.$$

While the feedback is based on the error under the P2D estimator, the network at each timeslot is optimized using

the mean-squared error loss function with respect to the error under the ground truth, $\mathbf{E}_t = \tilde{\mathbf{H}}_t - \gamma \hat{\mathbf{H}}_{t-1}$,

$$L_{\text{MSE}} = \frac{1}{N_{\text{batch}}} \sum_{i=1}^{N_{\text{batch}}} \|\mathbf{E}_t^{(i)} - \hat{\mathbf{E}}_t^{(i)}\|_2^2 \quad (8)$$

where i indexes over the N_{batch} samples of a training batch.

Figure 3 demonstrates the principle of differential encoding used with P2D estimates. Notably, both the BS and the UE need access to a copy of the decoder, $g_t(x)$, in order to derive the error term \mathbf{E}_t based on (7). Since both the encoder and the decoder are required on the UE side, we seek to design a differential encoding scheme with a small number of parameters.

A. CNN Autoencoders for CSI Feedback

Prior work utilized CNN autoencoders to implement a trainable differential encoding network for CSI estimation [11]. Using autoencoders in a differential encoding network, each timeslot t_i utilizes a CNN-based encoder ($f_i(x)$) and decoder ($g_i(x)$). Early work in deep learning-based CSI compression

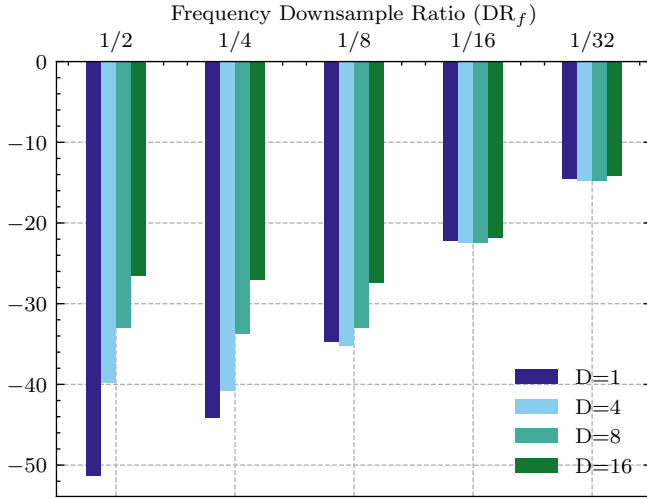


Fig. 5: P2D estimation performance under different frequency downsampling ratios (DR_f) and diagonal dimensions (D) for the Outdoor COST2100 dataset. Downsampling is done along the frequency axis.

concluded that convolutional autoencoders consistently outperformed traditional compressed sensing (CS) approaches [5].

In this work, we investigate two autoencoder networks to realize our differential encoding network. First, we utilize CsiNet Pro [13], an improved version of CsiNet which utilizes a symmetric encoder/decoder structure without residual connections, and ENet [14], another symmetric architecture applied independently to the real and imaginary channels to produce a complex-valued matrix. These two networks can be viewed at the bottom of Figure 4.

B. Iterative Optimization Networks for Compressed Sensing-based CSI Feedback

While CNN autoencoders have been dominant in CSI estimation, recent work from image processing has shown promise in using trainable CS algorithms based on CNNs. These works treat iterative CS algorithms as sequential networks by “unrolling” them into discrete blocks [15], [16]. Investigating unrolled CS algorithms for CSI estimation warrants consideration, as CS algorithms can have guaranteed convergence under mild sparsity conditions (in contrast with CNNs autoencoder approaches, which do not have such guarantees). Since CSI data exhibits sparsity in the delay domain, specifying an appropriate compressed sensing approach could provide appreciable performance gains in our differential CSI encoding architecture.

To exploit the temporal coherence of the MIMO channel, we propose to construct a differential encoding network using an unrolled optimization network based on a trainable version of the iterative shrinkage-thresholding algorithm (ISTA), called ISTANet+ [16]. See the top of Figure 4 for a diagram of ISTANet+. Denote the measurement matrix for the ISTANet+ as

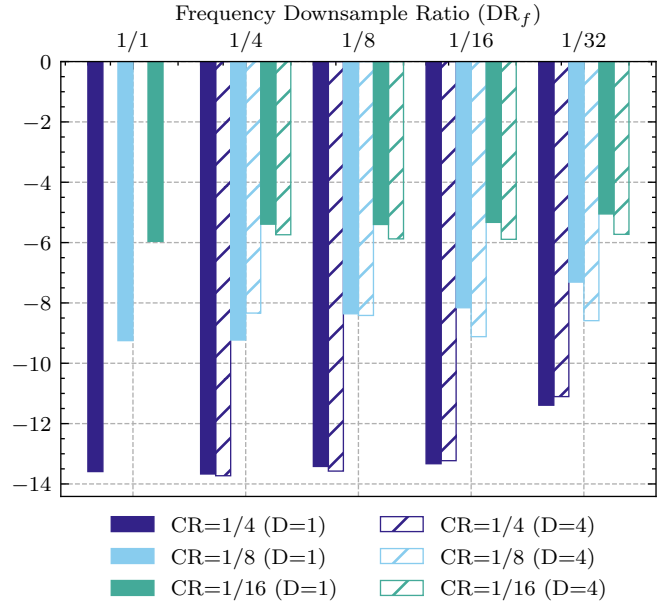


Fig. 6: Performance of ISTANet+ for multiple compression ratios using P2D estimates with different downsampling ratios (DR_f) for the Outdoor COST2100 dataset. Non-diagonal pattern ($D = 1$) is compared with a diagonal pattern of size $D = 4$. Performance for $DR_f = 1/1, D = 4$ is omitted since it is equivalent to the $DR_f = 1, D = 1$ case.

$$\Phi \in \mathbf{R}^{N_{\text{total}} \text{CR} \times N_{\text{total}}}. \quad (9)$$

For compressed sensing approaches, the measurement matrix is the equivalent of the ‘encoder’ for autoencoder approaches, i.e., $f(x) = \Phi x$. The ‘decoder’ consists of K iterations of the following update steps,

$$\begin{aligned} \mathbf{r}^{(k)} &= \mathbf{x}^{(k-1)} - \rho^{(k)} \Phi^\top (\Phi \mathbf{x}^{(k-1)} - \mathbf{y}) \\ \mathbf{x}^{(k)} &= \mathbf{r}^{(k)} + \mathcal{G}^{(k)} \left(\tilde{\mathcal{H}}^{(k)} \left(\text{soft} \left(\mathcal{H}^{(k)} (\mathcal{D}^{(k)} (\mathbf{r}^{(k)}), \theta^{(k)}) \right) \right) \right) \end{aligned} \quad (10)$$

where $\mathbf{y} = \Phi \mathbf{x}$, $\mathbf{x}^{(0)} = \mathbf{Q}_{\text{init}} \mathbf{y}$, and $\mathbf{Q}_{\text{init}} = \mathbf{X} \mathbf{Y} (\mathbf{Y} \mathbf{Y}^\top)^{-1}$. The initialization matrix \mathbf{Q}_{init} for the training data matrix $\mathbf{X} = [\mathbf{x}_1, \mathbf{x}_2, \dots, \mathbf{x}_{N_{\text{train}}}]$ and the training measurement matrix $\mathbf{Y} = [\mathbf{y}_1, \mathbf{y}_2, \dots, \mathbf{y}_{N_{\text{train}}}]$. ‘soft(\cdot)’ denotes the soft threshold function,

$$\text{soft}(x, \theta) = \text{sign}(x) \text{ReLU}(|x| - \theta). \quad (12)$$

$\mathcal{G}^{(k)}, \mathcal{D}^{(k)}, \mathcal{H}^{(k)}, \tilde{\mathcal{H}}^{(k)}$ indicate trainable nonlinear mappings (in this case, CNNs), and $\mathcal{H}^{(k)}, \tilde{\mathcal{H}}^{(k)}$ are subject to the symmetry constraint $\mathcal{H}^{(k)} \circ \tilde{\mathcal{H}}^{(k)} = \mathbf{I}$. In the proposed differential encoding scheme, we use an instance of ISTANet+ in the first timeslot, t_1 , with a large compression ratio such that $\text{CR}_{t_1} \geq \text{CR}_{t_i}$ for all $i > 1$. This choice in compression ratio allows us to initialize the network with a high-quality estimate at the first timeslot. Notably, the training data matrix,

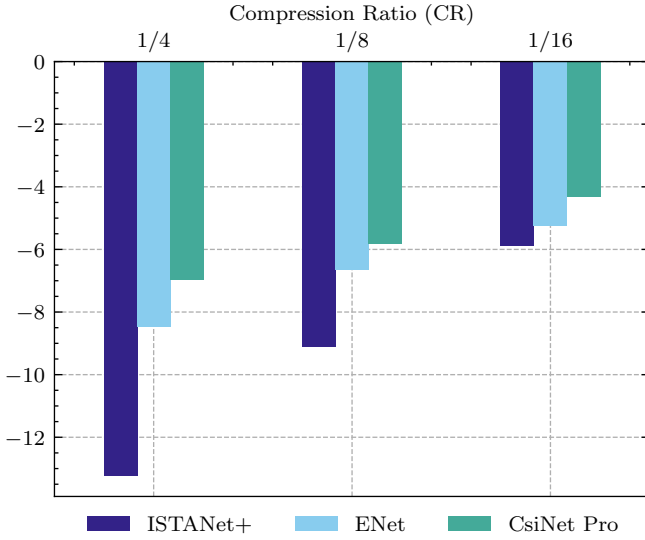


Fig. 7: Performance comparison for different feedback compression networks using P2D estimates ($DF_f = 1/16$, $D = 4$) for Outdoor COST2100 dataset.

\mathbf{X} , differs between timeslots. For the first timeslot, the data vectors \mathbf{x}_i are vectorized versions of the CSI matrices,

$$\mathbf{x}_j = \text{vec}(\tilde{\mathbf{H}}_1^{(j)}) \text{ for } j \in [N_{\text{train}}]. \quad (13)$$

However, the data vectors for all other timeslots are vectorized versions of the error matrices,

$$\mathbf{x}_j = \text{vec}(\tilde{\mathbf{E}}_i^{(j)}) \text{ for } j \in [N_{\text{train}}]. \quad (14)$$

Denote the parameters for ISTANet+ in the t_i -th timeslot as $\Theta_{t_i} = \{\mathcal{G}^{(k)}, \mathcal{D}^{(k)}, \mathcal{H}^{(k)}, \tilde{\mathcal{H}}^{(k)}, \theta^{(k)}, \rho^{(k)}\}_{k=1}^K$. The loss function is a weighted sum of the MSE and the symmetry constraint, i.e.,

$$L(\Theta_{t_i}) = L_{\text{MSE}} + \gamma L_{\text{sym}} \quad (15)$$

$$L_{\text{MSE}} = \frac{1}{N_{\text{batch}} N_{\text{total}}} \sum_{i=1}^{N_{\text{batch}}} \|\mathbf{x}_i^{(K)} - \mathbf{x}_i\|_2^2 \quad (16)$$

$$L_{\text{sym}} = \frac{1}{N_{\text{batch}} N_{\text{total}}} \sum_{i=1}^{N_{\text{batch}}} \sum_{k=1}^K \|\tilde{\mathcal{H}}^{(k)}(\mathcal{H}^{(k)}(\mathbf{x}_i)) - \mathbf{x}_i\|_2^2 \quad (17)$$

where $N_{\text{total}} = N_b N_t$ is the size of the truncated CSI matrix, K is the number of iterations in ISTANet+, and N_{batch} is the batch size used during training. As denoted in equations (13) and (14), the vectors \mathbf{x}_i depend on the timeslot.

V. RANDOM PHASE AUGMENTATION

Prior work leveraged the truncated delay domain, which allowed them to save large datasets of truncated CSI matrices. In order to acquire P2D estimates for different values of DR_f and D , we must store the full frequency domain CSI matrices. These full matrices can be prohibitively expensive to store under typical system parameters, meaning we need to use

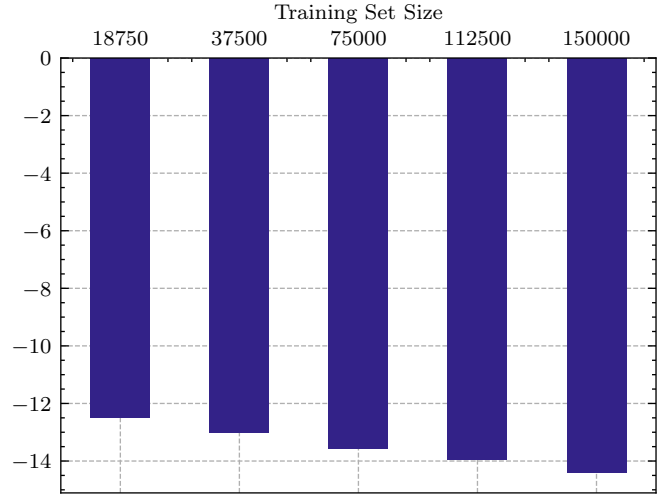


Fig. 8: ISTANet+ with P2D performance under different augmented dataset sizes after phase randomization for the Outdoor COST2100 dataset. Downsampling is done along the frequency axis.

a smaller dataset. Since successful training of deep neural networks depends on a large number of training samples, we utilize a random phase augmentation on our smaller training data. For each sample in the training set, we sample a random phase from a uniform distribution, $\theta \sim \mathcal{U}(-\pi, \pi)$, and we rotate all the elements in a given CSI matrix by this phase,

$$\mathbf{H}_{\text{augmented}}^{(i,j)} = \mathbf{H}^{(i,j)} e^{-j\theta} \quad \forall i \in [N_t], j \in [M_f]. \quad (18)$$

define a *phase augmentation factor*, N_{phase} , which is a multiplicative factor denoting the size of the training dataset after performing phase augmentation. For example, if we begin with a training set of size 5000, then $N_{\text{phase}} = 2$ would result in an augmented dataset of size 10,000, meaning each sample in the training set is augmented once. More generally, each sample in the training set is augmented $N_{\text{phase}} - 1$ times.

VI. RESULTS

TABLE I: Parameters for COST2100 model in this work.

Environment	Outdoor
Num. gNB Antennas (N_b)	32
Truncation Value (N_t)	32
Num. Subcarriers (N_f)	1024
Downsampled Subcarriers (M_f)	[512, 256, 128, 64]
Carrier Frequency	300 MHz
UE Starting Position	400 m \times 400 m
Num. Channel Samples (N)	10^4

We perform experiments using the COST2100 Model in an Outdoor scenario [17]. Table I summarizes the COST model parameters used to generate the Outdoor dataset. Importantly, the number of channel samples in the dataset is lower than the number used in similar works. A smaller dataset is necessary because we store full CSI matrices without truncating any

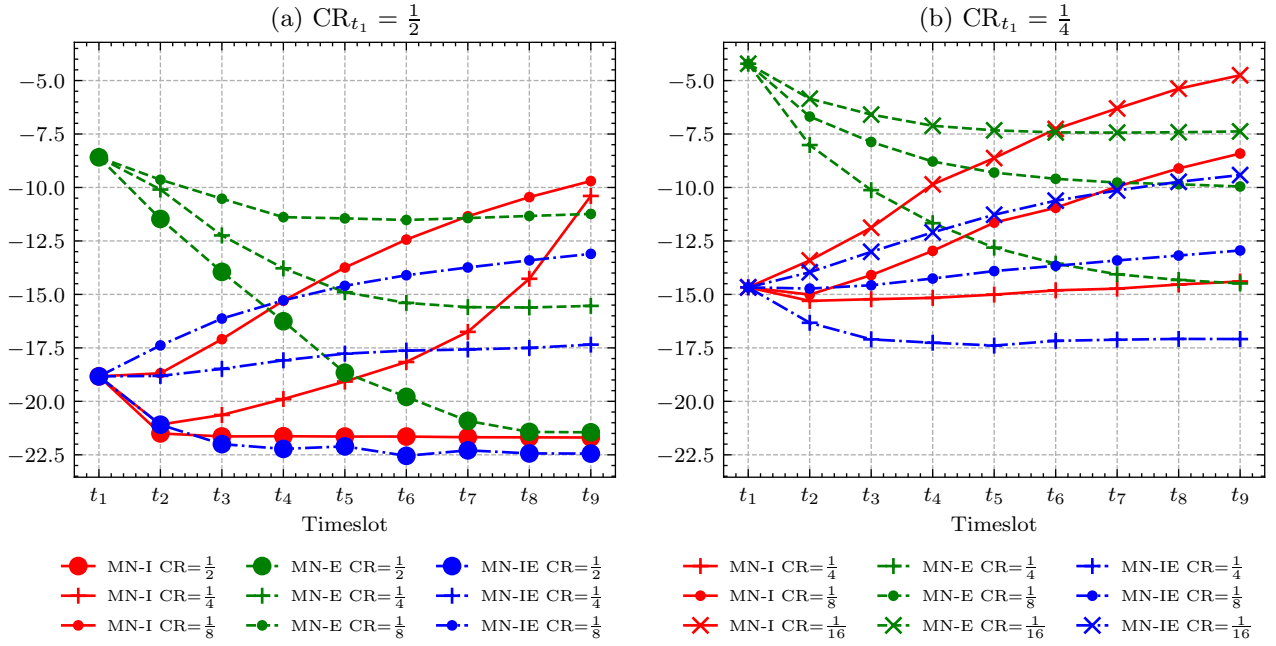


Fig. 9: Compressive CSI estimation using differential encoding and the linear P2D estimator ($M_f = 128, DR_f = \frac{1}{8}, D = 4$). MarkovNet-ISTA (MN-I), MarkovNet-ENet (MN-E), and MarkovNet-ISTA-ENet (MN-IE) are tested using two different compression ratios in the first timeslot, $CR_{t_1} \in [\frac{1}{2}, \frac{1}{4}]$.

subcarriers, which requires 32 times more space to store. For all networks, we utilize spherical normalization [13], and we test the networks using the following configurations:

- **ISTANet+**: We train the network described in Section IV-B for 100 epochs using the ADAM optimizer. The network utilizes 32 latent channels, 9 blocks, and a symmetry weight parameter of $\gamma = 10^{-3}$.
- **ENet**: The network hyperparameters are identical to those described in the original paper [14]. Since the training procedure was not described, we chose one which converged in a reasonable number of epochs (200 epochs, learning rate of 10^{-3}). As per the original paper, we train the network on the real channel data from the training set, then we report the validation loss by using the network on the real and imaginary channels from the validation set. We utilize $N_f = 32$ latent convolutional channels since this configuration achieved the best performance in the original paper.
- **CsiNet Pro**: The hyperparameters and training process are identical to those described in the original paper [13].

We use a 75% (25%) training (validation) split, yielding 7500 training samples (2500 validation samples). Unless stated otherwise, we augment the training set using $N_{\text{phase}} = 10$, yielding an augmented dataset of 75,000 samples.

A. Accuracy of P2D Estimator

To provide a bound on the estimation performance at the gNB, Figure 5 shows the accuracy of the P2D estimator at the UE (i.e., before compression and feedback). The performance of the P2D estimator under multiple diagonal sizes (D) is

shown. For all tested frequency downsampling ratios (DR_f), the accuracy of the P2D estimator is substantial, with the smallest $DR_f = \frac{1}{32}$ achieving about -14 dB. For increasing D , the error of the P2D estimator increases; however, the difference in performance for different values of D becomes negligible at more aggressive downsampling ratios, $DR_f \in [\frac{1}{16}, \frac{1}{32}]$. The accuracy of the P2D estimator implies that it will perform well with compressive CSI feedback networks.

B. Accuracy of Compressive Networks with P2D Estimates

In these experiments, we use the P2D estimate as the input to different compressive CSI feedback networks. In this work, we propose to use the unrolled reconstruction network, ISTANet+ [16], as described in Section IV-B. In Figure 6, we assess the performance of ISTANet+ across multiple values of DR_f and CR. Comparing $DR_f = \frac{1}{1}$ to $DR_f = \frac{1}{16}$, the accuracy of ISTANet+ is remarkably stable, increasing negligibly for $CR = \frac{1}{4}$ and by only 1 dB for $CR = \frac{1}{16}$.

To provide a baseline for ISTANet+, we also compare the performance of ISTANet+ with two autoencoder-based CSI compression networks, CsiNet Pro [13] and ENet [14]. Figure 7 shows the performance comparison between all networks for the same DR_f and D . Across all compression ratios, ISTANet+ achieves a better NMSE than the autoencoder approaches.

C. Phase Augmentation Ablation

Using random phase augmentation as described in Section V, we assess the influence of different sized training sets on validation accuracy. Starting with a training set of size

18750, we augment the dataset by $N_{\text{phase}} \in [2, 4, 6, 8]$, yielding training sets of size 37500, 75000, 112500, and 150000. We train ISTANet+ ($\text{CR}=\frac{1}{4}$) without P2D (i.e., perfect delay domain data) on each of these training sets, and we report the validation loss on the same 6250 samples. The resulting validation accuracy can be seen in Figure 8. As expected, the accuracy improves appreciably as the size of the augmented training set is increased.

D. Differential Encoding with P2D Estimates

Figure 9 shows the performance of differential encoding when using either ISTANet+ and ENet at each timeslot, which are respectively named MarkovNet-ISTA (MN-I) and MarkovNet-ENet (MN-E). For all versions of MarkovNet, CR_{t_1} is the compression ratio in the first timeslot and CR is the compression ratio for all following timeslots. ISTANet+ has the benefit of providing accuracy in the first timeslot, while ENet is better at compressing the residual in each following timeslot. Based on this observation, we also test a version of MarkovNet which uses ISTANet+ in the first timeslot then ENet in the following timeslots, which we call MarkovNet-ISTA-ENet (MN-IE). For the networks where $\text{CR}_{t_1} = \text{CR}$, MN-IE can outperform MN-I, indicating that a combination of architectures can be better than a single architecture.

VII. DISCUSSION

In this work, we present the P2D estimator, a linear estimator for the truncated angular-delay domain CSI based on downsampled spatial-frequency CSI. The P2D estimator provides accurate delay domain CSI based on practical CSI-RS pilot allocations that adhere to the LTE standard. Furthermore, we demonstrate that CSI estimates from the P2D estimator provide a suitable input to trainable CS networks and autoencoder networks. Finally, we propose a differential encoding network, MarkovNet-ISTA-ENet, which combines a trainable CS network with multiple autoencoders to better leverage the high initial accuracy of the former and the error-compressing capabilities of the latter.

REFERENCES

- [1] A. Goldsmith, S. A. Jafar, N. Jindal, and S. Vishwanath, "Capacity limits of mimo channels," *IEEE Journal on Selected Areas in Communications*, vol. 21, no. 5, pp. 684–702, June 2003.
- [2] F. Kaltenberger, H. Jiang, M. Guillaud, and R. Knopp, "Relative Channel Reciprocity Calibration in MIMO/TDD Systems," in *2010 Future Network Mobile Summit*, June 2010, pp. 1–10.
- [3] D. Mi, M. Dianati, L. Zhang, S. Muhaidat, and R. Tafazolli, "Massive mimo performance with imperfect channel reciprocity and channel estimation error," *IEEE Trans. Communications*, vol. 65, no. 9, pp. 3734–3749, 2017.
- [4] Q. Gao, F. Qin, and S. Sun, "Utilization of channel reciprocity in advanced mimo system," in *2010 5th International ICST Conference on Communications and Networking in China*, Aug 2010, pp. 1–5.
- [5] C. Wen, W. Shih, and S. Jin, "Deep Learning for Massive MIMO CSI Feedback," *IEEE Wireless Communications Letters*, vol. 7, no. 5, pp. 748–751, Oct 2018.
- [6] Z. Lu, J. Wang, and J. Song, "Multi-resolution csi feedback with deep learning in massive mimo system," in *ICC 2020 - 2020 IEEE International Conference on Communications (ICC)*, 2020, pp. 1–6.
- [7] M. Hussien, K. K. Nguyen, and M. Cheriet, "PRVNet: Variational autoencoders for massive MIMO CSI feedback," *arXiv*, 2020.

- [8] Y. Sun, W. Xu, L. Fan, G. Y. Li, and G. K. Karagiannidis, "Ancinet: An efficient deep learning approach for feedback compression of estimated csi in massive mimo systems," *IEEE Wireless Communications Letters*, vol. 9, no. 12, pp. 2192–2196, 2020.
- [9] Z. Liu, L. Zhang, and Z. Ding, "Exploiting Bi-Directional Channel Reciprocity in Deep Learning for Low Rate Massive MIMO CSI Feedback," *IEEE Wireless Comm. Letters*, vol. 8(3), pp. 889–892, 2019.
- [10] T. Wang, C. Wen, S. Jin, and G. Y. Li, "Deep learning-based csi feedback approach for time-varying massive mimo channels," *IEEE Wireless Communications Letters*, vol. 8, no. 2, pp. 416–419, April 2019.
- [11] Z. Liu†, M. del Rosario†, and Z. Ding, "A Markovian Model-Driven Deep Learning Framework for Massive MIMO CSI Feedback," *IEEE Transactions on Wireless Communications*, pp. 1–1, 2021.
- [12] H. Asplund, D. Astely, P. von Butovitsch, T. Chapman, M. Frenne, F. Ghasemzadeh, M. Hagström, B. Hogan, G. Jöngren, J. Karlsson, F. Kronstedt, and E. Larsson, "Chapter 8 - 3GPP Physical Layer Solutions for LTE and the Evolution Toward NR," in *Advanced Antenna Systems for 5G Network Deployments*. Academic Press, 2020, pp. 301–350. [Online]. Available: <https://www.sciencedirect.com/science/article/pii/B9780128200469000083>
- [13] Z. Liu, M. del Rosario, X. Liang, L. Zhang, and Z. Ding, "Spherical normalization for learned compressive feedback in massive MIMO CSI acquisition," in *IEEE ICC Workshops*, 2020, pp. 1–6.
- [14] Y. Sun, W. Xu, L. Liang, N. Wang, G. Y. Li, and X. You, "A lightweight deep network for efficient csi feedback in massive mimo systems," *IEEE Wireless Communications Letters*, 2021.
- [15] Y. Yang, J. Sun, H. Li, and Z. Xu, "Deep adm-net for compressive sensing mri," in *Proceedings of the 30th international conference on neural information processing systems*, 2016, pp. 10–18.
- [16] J. Zhang and B. Ghanem, "Ista-net: Interpretable optimization-inspired deep network for image compressive sensing," in *Proceedings of the IEEE conference on computer vision and pattern recognition*, 2018, pp. 1828–1837.
- [17] L. Liu, C. Oestges, J. Poutanen, K. Haneda, P. Vainikainen, F. Quitin, F. Tufvesson, and P. D. Doncker, "The COST 2100 MIMO channel model," *IEEE Wireless Comm.*, vol. 19, no. 6, pp. 92–99, Dec. 2012.